An electrochemically active textile current collector with a high areal capacity and a strong energy recovery effect using an interfacial interaction assembly

Euiju Yong [a],[†], Donghyeon Nam [a],[†], Yangsoo Kim [d], Kwangsoo Kim [e], Byung-Hyun Kim [e], Yongmin Ko [f], Jinhan Cho [a],[b],[c],[*]

[a] Department of Chemical and Biological Engineering, Korea University, 145 Anam-ro, Seongbuk-gu, Seoul 02841, Republic of Korea
[b] KU-KIST Graduate School of Converging Science and Technology, Korea University, 145 Anam-ro, Seongbuk-gu, Seoul 02841, Republic of Korea
[c] Soft Hybrid Materials Research Center, Advanced Materials Research Division, Korea Institute of Science and Technology (KIST), 5 Hwarang-ro 14-gil, Seongbuk-gu, Seoul 02792, Republic of Korea
[d] Korea Basic Science Institute Jeonju Center, Jeonju 54907, Republic of Korea
[e] Computational Science & Engineering Laboratory Korea Institute of Energy Research 152 Gajeong-ro, Yuseong-gu, Daejeon 34129, Republic of Korea
[f] Division of Energy Technology, Daegu Gyeongbuk Institute of Science and Technology (DGIST), 333 Techno Jungang-daero, Hyeonpung-eup, Dalseong-gun, Daegu 42988, Republic of Korea

ARTICLE INFO

ABSTRACT

Conventional current collectors in lithium-ion batteries (LIBs) are generally nonactive components. However, enhancing their electroactive properties and increasing the electroactive surface area can significantly improve the areal energy performance of next-generation battery electrodes. Herein, we introduce an electrochemically active textile current collector that delivers high energy storage performance, achieved through interfacial interaction assembly-induced electroplating. We first prepared metal nanoparticle/multiwalled carbon nanotube multilayer-incorporated cotton textiles using complementary interaction-mediated layer-by-layer assembly, and subsequently electroplated them with Cu. The resulting textile exhibited a high areal capacity of $\sim$3.27 mA h cm^{-2} at 0.875 mA cm^{-2}, excellent cycling stability, and a strong energy recovery effect, thanks to the synergistic contributions of the large active surface area of the fibril structure, the robust interfacial assembly, and the formation of a metal oxide NP/pseudocapacitive polymeric gel-like phase at the electrode/electrolyte interface. Moreover, when incorporating $Li_4Ti_5O_{12}$ with a theoretical capacity of 175 mA h g^{-1} into our textile current collector, the specific capacity and areal capacity of the LIB anode can be increased up to $\sim$573 mA h g^{-1} and 8.60 mA h cm^{-2} (at 15 mg cm^{-2} LTO), respectively, outperforming those of previously reported LTO-based anodes.

1. Introduction

The rapid evolution and tremendous growth of portable electronics have fueled extensive research efforts towards developing higher-performance energy storage electrodes [1–15], mainly rechargeable lithium-ion battery (LIB) electrodes [1–12,15] that are lighter, mechanically stable, and have longer lifetimes with higher areal performance indexes (i.e., areal capacity, areal energy density, and areal power density). Particularly, most studies on improving energy performance, such as energy density and rate capability, have focused on

developing and designing electrochemically active components such as electrode materials. However, comparatively little attention has been paid to current collectors, which do not contribute to the capacity.

Typically, commercial battery electrodes use thickly coated active materials on nonporous metal-foil-based current collectors (Cu foil for the anode and Al foil for the cathode) [3–7] to achieve higher energy density per unit area. However, such electrodes face trade-offs between areal capacity and mechanical stability, and between areal capacity and rate capability. Additionally, a high mass loading of active materials with low electrical conductivity (or increased electrode thickness)

significantly decreases the rate capability, hampering both high areal energy and high power density. Furthermore, thick active materials tend to delaminate from the current collector due to increased residual stress between the coating components and the current collector under various external mechanical stimuli [6–8].

To address these issues, more recently reported studies have focused on exploiting fibril-type textile current collectors[16–31] that can function as a large-area energy reservoir for active materials, reduce the

charge transfer resistance within electrodes through numerous conductive fibril networks, and allow for stress relief. Insulating textile substrates can be converted to conductive textiles through high-temperature-based carbonization [18,19], and physical incorporation of conductive materials such as multiwalled carbon nanotubes (MWCNTs) and carbon fibers [20–22]. However, most conductive textiles reported to date display relatively high electrical resistances (> 30 $\Omega\,sq^{-1}$) due to the low electrical conductivity of conductive components,
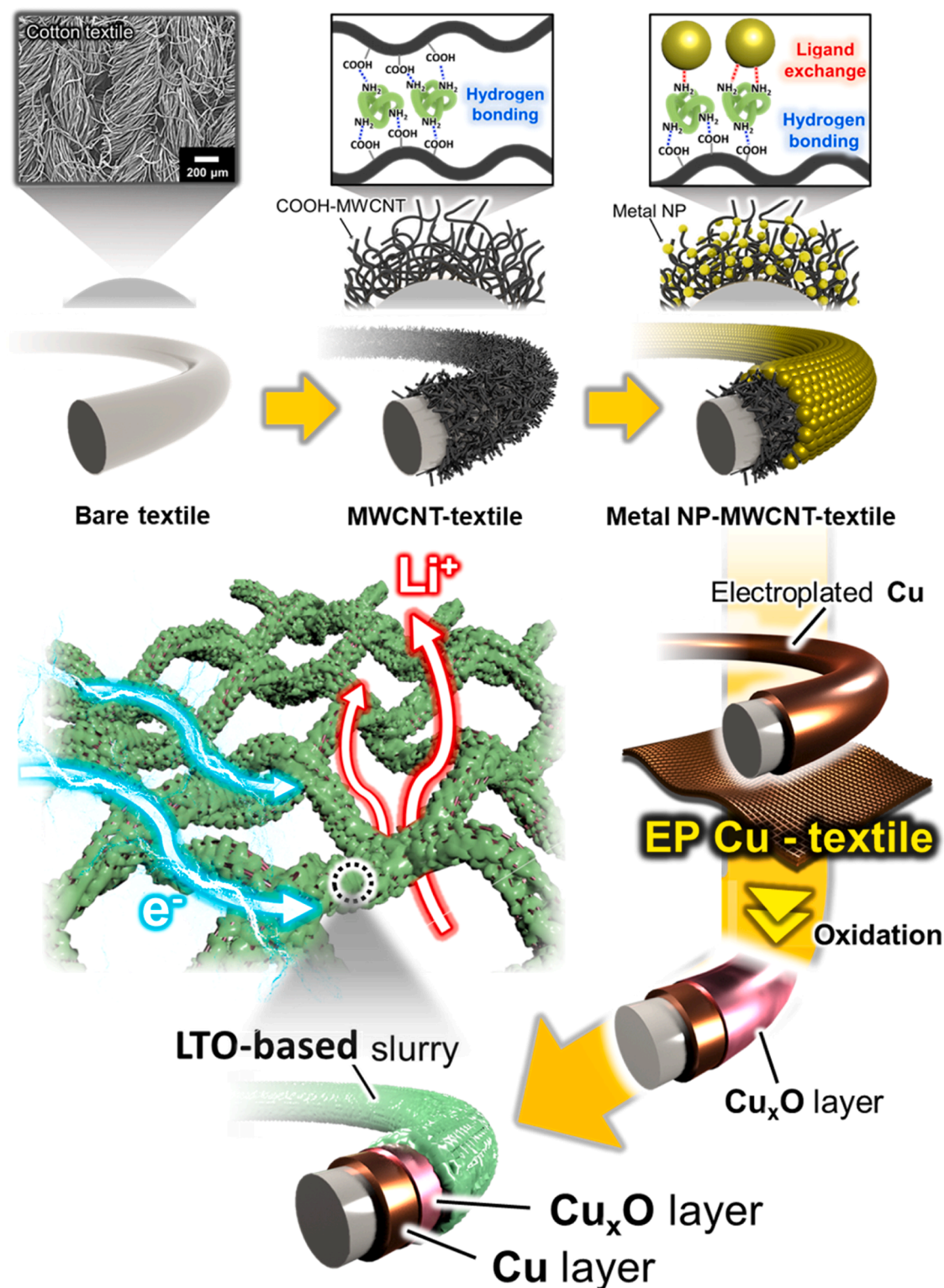
Scheme 1. Shematic illustration for the preparation of Cu-plated textile electrode using interfacial interaction assembly-induced Cu electroplating.

the aggregations and the numerous contact resistances between neighboring conductive components. Additionally, their mechanical flexibility and electrical/electrochemical stability are seriously restricted by poor interfacial interactions between textile and conductive components and between neighboring conductive components.

As an alternative, metal textile-based current collectors (specifically Cu, Ni, and Al) with excellent electrochemical stability, large surface area, and high economic feasibility can be applied to commercial LIB electrodes. However, preparing a high-quality metal textile remains a difficult and challenging task. The conventional chemical reduction process[23-26,28-30] has been mainly used for the preparation of metal textiles, but it has induced unevenly distributed metal aggregation along with relatively low electrical conductivity ($> 0.5 \, \Omega \, sq^{-1}$) compared to bulk-metal conductivity. This is due to the extremely rapid chemical reduction of metal ions and the presence of organic impurities in the metal precursors, resulting in a significant decrease of charge transfer kinetics, surface area, and operational stability. These critical problems have limited the effectiveness of metal textiles as current collectors for high-performance LIB electrodes. Although recent studies aim to effectively utilize current collectors, research on inactive current collectors has mainly focused on designing structural and physical properties to improve charge transfer kinetics and mass loading of active components. As a result, these approaches are limited to the theoretical capacity of the active materials due to their strong dependence on electrochemical properties. To overcome this fundamental issue, a new paradigm approach is highly required to impart electrochemical activity to the current collector itself.

Herein, we introduce an electrochemically active textile current collector with high energy performance using conductive multilayer assembly-induced electroplating (Scheme 1). Our textile current collector (specifically Cu textile) exhibits a considerably high areal capacity of ~3.27 mA h cm^{-2} (at 0.875 mA cm^{-2}) and unprecedentedly high energy recovery effect/operational stability (93.9% of the initial capacity after ~2000 cycles) without additional active materials. When $Li_4Ti_5O_{12}$ (LTO) is incorporated into our textile current collector, the specific and areal capacities of the overall electrode are increased. Although it was reported that the additional deposition of Cu oxide layer onto the chemical reduction-induced Cu textile could be used as Cu-textile anode, the areal capacity and cycling stability of the overall electrode did not exceed 2 mA h cm^{-2} and 120 cycles, respectively [28, 31,32]. Moreover, there were no information about the areal performance of the chemical reduction-induced Cu textile itself. To our knowledge, the exceptionally high performance of our Cu textile/LTO-incorporated textile electrode as well as MWCNT multilayer-induced electroplating approach have never been reported to date. Furthermore, we highlight that our approach can be expanded to the preparation of various metal textile current collectors, such as Ni and Al textiles, as well as Cu textiles.

For this study, we used an unconventional layer-by-layer (LbL) assembly to deposit MWCNT multilayers and metal NPs onto cotton textiles using small molecule linkers, reducing contact resistance between conductive components. This approach allowed for the conversion of insulating cotton textiles into conductive textiles with a sheet resistance of ~ 7.6 Ω sq^{-1}, which were further electrodeposited with Cu to create metallized Cu-textiles with a sheet resistance of ~0.08 Ω sq^{-1}. The resulting Cu textiles have high mechanical flexibility and bulk metal-like electrical properties due to favorable interfacial interactions between the conductive components, multilayers, and textile substrate.

Furthermore, our Cu-textile exhibited a high areal capacity without additional active materials due to the strong negative fading effect and the widespread formation of an outermost Cu oxide layer with a high theoretical specific capacity. The formed electroplated Cu textile (EP Cu-textile) with bulk metal-like electrical properties (~ 0.08 Ω sq^{-1}) exhibited an unprecedentedly high areal capacity (~3.27 mA h cm^{-2} at 0.875 mA cm^{-2}) and an excellent negative fading effect (~93.9% of the initial capacity after approximately 2000 cycles). Particularly, strong

energy recovery effect was mainly due to the generation of nanosized Cu particles during the lithiation process, which catalyze the formation of a polymeric gel-like phase and the reaction between Cu and Li_2O, along with a newly formed 3D open structure. These phenomena were also confirmed by Density Functional Theory (DFT) calculations.

To further demonstrate the practical effectiveness of our unique current collectors further, we additionally deposited LTO-based active materials onto the Cu-textile (for the anode). Thanks to the electrochemical activity of EP Cu-textile, the resulting anode showed exceptionally high energy storage performance (specific capacity ~573 mA h g^{-1} $_{LTO}$), surpassing the theoretical value (~175 mA h g^{-1}) of LTO. This indicates a remarkable potential of EP Cu-textile as an active current collector. Additionally, the formed electrodes' areal performance indexes, particularly the total areal capacity (8.60 mA h cm^{-2} at 15 mg cm^{-2} LTO and current density of 0.875 mA cm^{-2}) and rate capability, were significantly increased compared to those of conventional textile-based LTO electrodes [8,33-35] and nonporous Cu foil-based LTO electrodes [8,23,36]. Our approach can overcome the limitations of existing current collectors and provide an effective tool for developing and designing a variety of electrochemical and LIB electrodes, especially considering the notable areal capacity of the formed Cu-textile current collector itself.

2. Results

2.1. Preparation of conductive textiles

To develop a unique metallic textile-based current collector with a large specific surface area per unit textile volume, we first focused on the preparation and structural design of conductive seed multilayers, as are typically deposited onto insulating cotton textiles. To this end, MWCNTs with carboxylic acid (-COOH) functional groups were assembled with small molecule linkers containing three primary amine (-NH$_2$) groups (i. e., TREN), by layer-by-layer (LbL) assembly on cotton textile. Hydrogen bonding between the COOH groups of MWCNTs and NH$_2$ groups of TREN in ethanol (Fig. 1a) enabled growth of the layers, as confirmed by Fourier transform infrared (FTIR) spectroscopy. In Particular, the use of the extremely small TREN as a linker allowed us to significantly reduce the contact resistances between neighboring conductive COOH-MWCNTs and further decrease the volume of the conductive seed multilayers, representing an improvement over the use of bulky linkers such as NH$_2$-functionalized MWCNTs or poly(ethylene imine). On the basis of this interfacial hydrogen-bonding interaction, the proportions of (COOH-MWCNT/TREN)$_n$ multilayers loaded as a function of the bilayer number (n) were quantitatively investigated with a quartz crystal microbalance (QCM) based on the Sauerbrey equation. According to the results (Fig. 1b), the mass increased relatively linearly with the alternating deposition of layers, demonstrating the uniform and regular growth of LbL-assembled (COOH-MWCNT/TREN)$_n$ multilayers (abbreviated hereafter as n-MWCNT).

To ensure a continuous electron path, we increased the bilayer number of n-MWCNT multilayers from 5 to 50, the sheet resistance decreased from approximately 8×10^6 to 7×10^3 Ω sq^{-1} (2.8×10^{-6} to 2.4×10^{-3} S cm^{-1}) (Fig. 1c). The n-MWCNT multilayers evenly covered individual cellulose fibrils and expanded the surface area available for application of other materials. However, surface functionalization of MWCNTs by acid treatment (i.e., COOH-MWCNTs) led to partial breakdown of the electron paths (i.e., a change in C hybridization from sp [2] to sp [3] due to destruction of aromaticity) [37], which did not significantly lower the sheet resistance of the conductive seed textile despite an increased bilayer number of the COOH-MWCNT multilayers. This limited sheet resistance of MWCNT multilayers causes poor coating quality of metal layer on the textile (Fig. S22).

To investigate how we might further enhance the process efficiency as well as the electrical conductivity, 10 nm Au nanoparticles (NPs) stabilized with tetra(octyl ammonium) bromide (TOABr) were
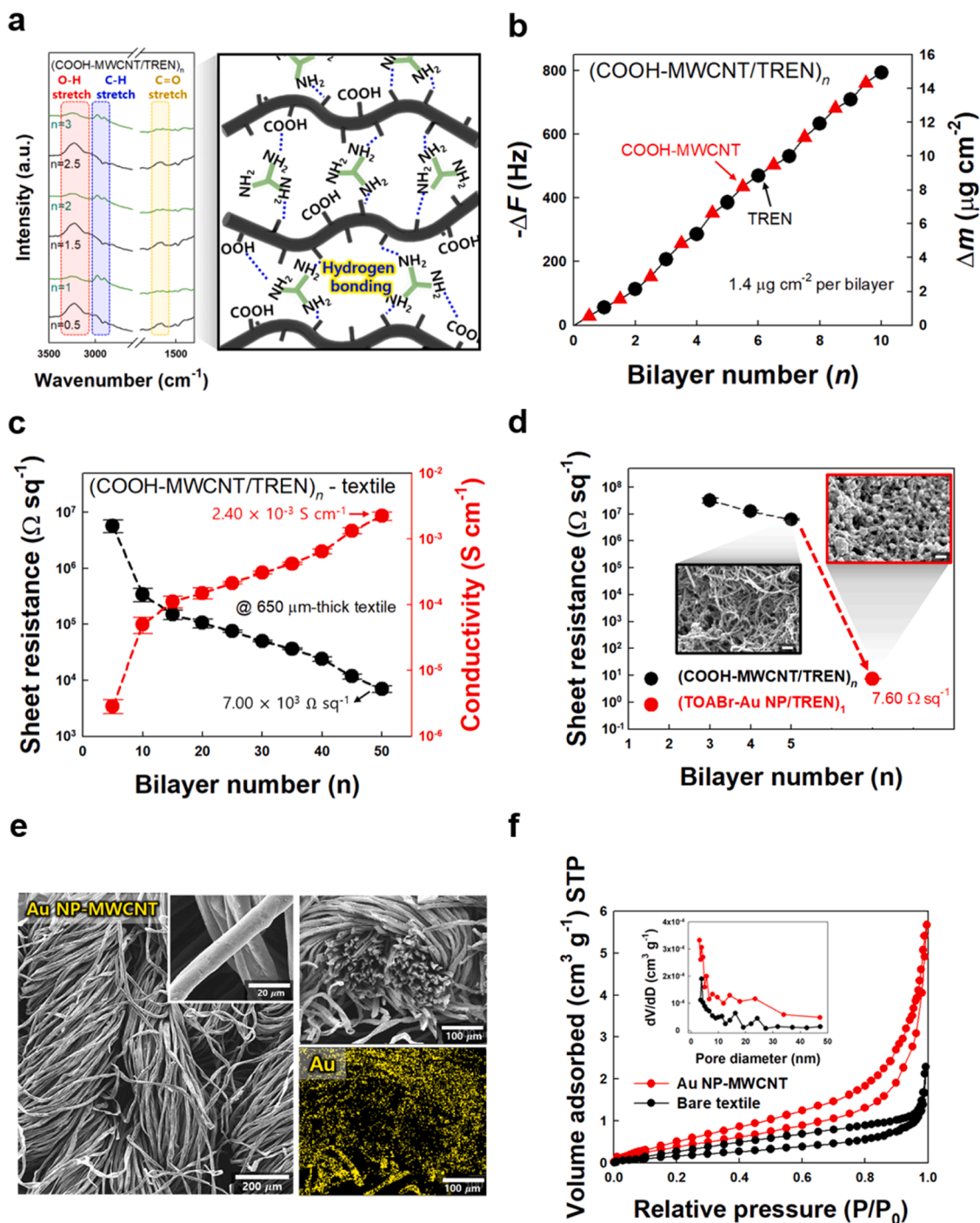
Fig. 1. Optimization of the conductive seed multilayers (i.e., (TOABR-Au NP/TREN)$_n$/5-MWCNT-textile where $n = 1$) on cotton textile. (a) FTIR spectra of the (COOH-MWCNT/TREN)$_n$ multilayers as a function of the number of bilayers (n; left) and a schematic illustration of interfacial interactions between COOH-MWCNTs and TREN (right). (b) QCM data of the (COOH-MWCNT/TREN)$_n$ multilayers as a function of the number of bilayers (n). (c) Sheet resistance and electrical conductivity of the (COOH-MWCNT/TREN)$_n$-textile as a function of the number of bilayers (n). (d) Sheet resistance of the (TOABr-Au NP/TREN)$_1$/5-MWCNT-textile (insets: FE-SEM images obtained before and after TOABr-Au NP deposition (scale bar, 500 nm)). (e) Planar and cross-sectional FE-SEM images and EDS maps of the (TOABr-Au NP/TREN)$_1$/5-MWCNT-textile. (f) N$_2$ adsorption-desorption isotherms for the bare textile and the (TOABr-Au NP/TREN)$_1$/5-MWCNT-textile (inset: pore size distribution).

assembled with TREN onto a 5-MWCNT multilayer-coated textile. The bulky TOABr ligands on the Au NP were easily replaced by amine moieties of TREN via covalent-bonding-induced ligand exchange during deposition, as confirmed by FTIR analysis (Fig. S1 in the supplementary material). The addition of this final bilayer decreased the sheet resistance from 8×10^6 Ω sq^{-1} to 7.6 Ω sq^{-1} (Fig. 1d) and increased the electrical conductivity (across the ~ 650 µm total thickness of the

textile) from 1.9×10^{-6} to 2.0 S cm^{-1}. The Au NPs did not significantly affect the porous structure of the cotton textiles (inset of Fig. 1d), suggesting that the ion diffusion properties and large surface area of the were maintained. Additionally, we confirmed that Au NPs were uniformly deposited onto the entire area ranging from the exterior to the interior of 5-MWCNT-textile with field emission scanning electron microscopy (FE-SEM) and energy dispersive X-ray spectroscopy (EDS)

(Figs. 1e and S26). Although the sheet resistance decreased as the number of TOABr-Au NP/TREN bilayers increased, the sheet resistance for one bilayer of TOABr-Au NP/TREN on a 5-MWCNT-textile was sufficiently low for the application of commercial electroplating methods to be feasible. Given that TREN linkers can significantly reduce the contact resistance, as mentioned above, and thereby induce the formation of robust coatings. Our findings imply that the electrical conductivities of textiles can be easily enhanced through LbL assembly of conductive nanomaterials (MWCNTs and metal NPs) on pristine textile. The specific surface area ($1.857 \ m^2 \ g^{-1}$) of the (TOABr-Au NP/TREN)$_1$/5-MWCNT-textile (shortly, Au NP-MWCNT-textile) was 2.23 times greater than that ($0.830 \ m^2 \ g^{-1}$) of bare cotton textile as confirmed with the Brunauer-Emmett-Teller (BET) method (Fig. 1f). Thus, the insulating cotton textile was successfully converted to the conductive textile with an increased specific surface area. Furthermore, it is worth noting that our approach (ligand exchange reaction-based deposition) can effectively be applied to various metal NPs, including Cu NP, for the formation of high-quality metallic seed layer of the textile (Fig. S23).
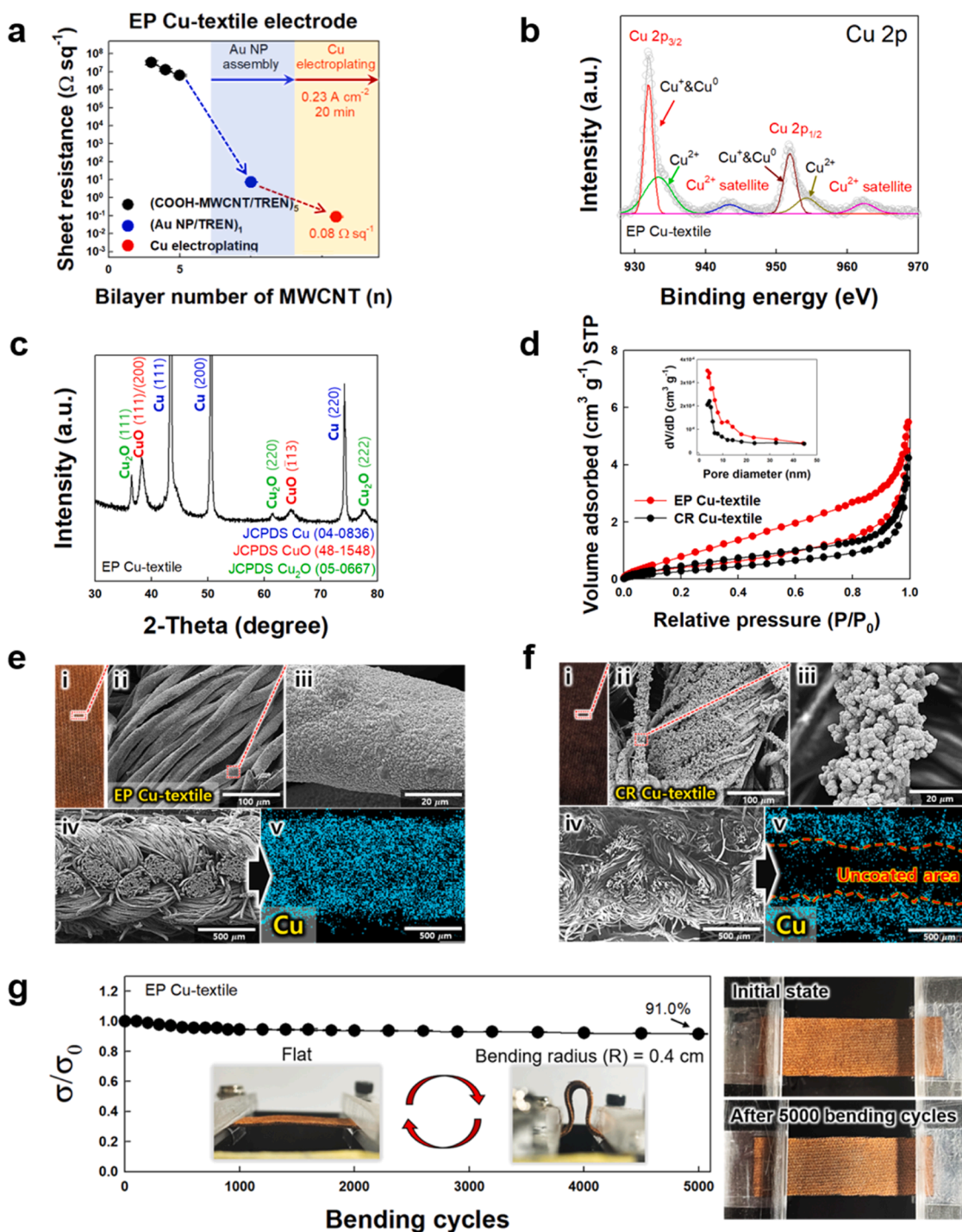

Fig. 2. Preparation of EP Cu-textile. (a) Sheet resistance (b) XPS spectrum, and (c) XRD spectrum of an EP Cu-textile. (d) N_2 adsorption-desorption isotherms of the EP Cu-textile and CR Cu-textile (inset: pore size distributions). (e) (i) Photographic image, (ii, iii) planar and (iv) cross-sectional FE-SEM images and EDS maps of the EP Cu-textile. (f) Photographic image, (ii, iii) planar and (iv) cross-sectional FE-SEM images and EDS maps of the CR Cu-textile. (g) Electrical stability tests of EP Cu-textile and photograph image of the EP Cu-textile before and after 5000 cycle-bending test with bending radius of 0.4 cm (right).

2.2. Preparation and characterization of EP Cu-textile current collectors

Copper electroplating with a two-electrode system was conducted on the Au NP-MWCNT-textile (0.5 cm × 2.5 cm) in aqueous electrolyte, which reduced the sheet resistance to 0.08 Ω sq^{-1} (Fig. 2a). In this case, it should be noted that the outermost TREN layer of Au NP-MWCNT-textile has a high affinity for electroplated Cu layer due to the covalent-bonding interaction between NH_2 groups of TREN and Cu layer.

Time-of-flight secondary ion mass spectrometry (TOF-SIMS) performed after post-annealing (Fig. S2 in the supplementary material), confirmed the presence of copper oxides (CuO/Cu_2O mixed phase) on the surface of the EP Cu-textile. For comparison, Cu-coated textiles were also prepared by chemical reduction process, one of the most widely used processes for depositing the metal layer onto textiles [24]. X-ray photoelectron spectroscopy (XPS) was used to investigate the electronic state of the EP Cu layer (Figs. 2b and S3 in the supplementary material) and chemical reduction-induced Cu layer (shortly, CR Cu layer) (Fig. S4 in the supplementary material). The Cu 2p XPS spectrum of the EP Cu layer contains sharp peaks at 934.2 and 954.1 eV corresponding to Cu $2p_{3/2}$ and Cu $2p_{1/2}$ binding energies, respectively. The Cu $2p_{3/2}$ and Cu $2p_{1/2}$ peaks for metallic Cu are typically located at 932.8 and 952.7 eV, the shifts to higher binding energies indicated the formation of copper oxides on the EP Cu layer. The presence of Cu^{2+} satellite peaks at 943.5 and 962.4 eV suggested that CuO and Cu_2O were formed on the outermost surface of the EP Cu layer [38–40]. In this case, the chemical compositions of the EP Cu layer were almost similar to those of CR Cu layer. The crystal structure of the EP Cu-textile was also investigated by X-ray diffraction (XRD) (Fig. 2c). The diffraction peaks at 43.3°, 50.4° and 73.6° were indexed to the (111), (200), and (220) planes of Cu phase (JCPDS file No. 04–0836), respectively. The weak diffraction peaks at 38.8°, 39.1°, and 56.7° corresponded to the (111), (200), (113) and (004) planes of CuO phase (JCPDS file No. 48–1548), and the peaks at 36.4° and 61.4° corresponded to the (111) and (220) planes of Cu_2O phase (JCPDS file No. 05–0667), respectively [41]. These results showed that a copper oxide layer was formed on the EP Cu-textile. In this case, the mass loading of copper oxides on the textiles was analyzed by the electropolishing method, which was measured to be 1.04 and 1.48 mg cm^{-2}, respectively (see Experimental section). Particularly, considering that electrochemically active copper oxides (CuO and Cu_2O with theoretical specific capacities of ~674 and ~375 mA h g^{-1}, respectively) were present on the surface of the EP Cu-textile, we speculated that the EP Cu-textile might act as an active component as well as a current collector and energy reservoir, and enhance the areal capacity of an LIB anode (the more details are discussed in the later part).

Unlike EP Cu-textile, the sheet resistance of the CR Cu-textile (where the coated Cu layer was approximately ~7 μm thick) exhibited relatively high sheet resistance of 2 Ω sq^{-1} mainly because of the nonuniform coating quality of Cu layers and residual organic impurities from CR (Fig. S5 in the supplementary material). Additionally, the surface area (2.151 m^2 g^{-1}) was much greater for the EP Cu-textile than for the CR Cu-textile (1.322 m^2 g^{-1}) or the Au NP-MWCNT-textile (1.857 m^2 g^{-1}) (Fig. 2d), due to formation of a thin layer of EP Cu with highly uniform but protuberant nanostructure on the cotton fibrils (Fig. 2e), which was in stark contrast to the CR Cu-textile with agglomerated Cu and uncoated regions (Fig. 2f) as confirmed by FE-SEM and EDS analysis.

Furthermore, the robustness of the EP Cu- and CR Cu-textiles was tested by measuring their electrical conductivity under repeated bending cycles (Fig. 2g). After 5000 bending cycles (bending radius (R) ~ 0.4 cm), the EP Cu-textile maintained 91.0% of its initial conductivity. Additionally, the dense and uniform Cu layer maintained its electrical properties and structural integrity during various mechanical deformations such as bending and folding (Fig. S6 in the supplementary material) without noticeable delamination or cracking, which suggested possible applications in energy storage systems with mechanical flexibility. In contrast, the electrical conductivity of the CR Cu-textile rapidly

decreased during the same bending cycle test (Fig. S7 in the supplementary material) due to poor interfacial interactions between the CR Cu layer and textile and between aggregated Cu clusters. These results showed that the EP Cu-textile maintained its mechanical and electrical properties without notable loss even after many mechanical deformations. Furthermore, it should be noted that Au NP-MWCNT-textile can be easily converted to various other metal textiles such as Ni- and Al-textiles as well as Cu-textile (Fig. S8 in the supplementary material).

2.3. Electrochemical properties of Cu-based current collectors

To investigate the electrochemical performance of the EP Cu-textile, cycling voltammetry (CV) was performed with the EP Cu-textile at a scan rate of 0.1 mV s^{-1} over the voltage range of 0.01–3 V (Fig. S9 in the supplementary material). In the first discharge, reduction peaks at approximately 2.17, 1.63, and 0.61 V corresponded to formation of $Cu_{1-x}^{II}Cu_x^IO_{1-x/2}$ ($0 \leq x \leq 0.4$), partial reduction of CuO to Cu_2O (Eq. (1)), and subsequent conversion of Cu_2O into Cu and Li_2O (Eq. (2)), respectively [42–45].

$$CuO \ 2Li^+ + 2e^- \rightarrow Cu_2O + Li_2O \qquad (1)$$

$$Cu_2O \ 2Li^+ + 2e^- \rightarrow Cu + \ Li_2O \qquad (2)$$

Oxidation peaks at 1.01, 1.74, and 2.75 V were caused by partial decomposition of the organic layer of Li_2O (~ 1.01 V), oxidation of Cu to Cu_2O (~1.74 V) and partial oxidation of Cu_2O to CuO (~ 2.75 V), respectively. The Au NPs beneath the EP Cu-layer had a strong affinity for Li ions, and acted as lithiophilic nucleation seeds for the formation of a new Li-Au phase (see the reduction peak at approximately 0.1 V). The formed Li-Au phase was oxidized reversibly with three strong peaks at 0.2, 0.37, and 0.49 V under successive anodic sweeps [46]. However, during repeated electrochemical cycling, significant degradation of the electrochemical properties of the Li-Au phase was observed; this was also observed in the CV curves of the Au NP-MWCNT-textile (Fig. S10 in the supplementary material). These phenomena imply that Au NPs activated only during the first few cycles. Furthermore, our results suggest the possibility that, without any additional chemical treatment, the EP Cu-textile could be used as an active material for anodes as well as current collectors due to the large specific surface area of the copper oxide layer. Although the EP Cu-textile exhibited excellent electrochemical activity as a fascinating LIB anode, it is worth noting that the other metals such as Ni or Al can also effectively applied in our system depending on the purpose of the electrode (Fig. S27).

The formation of a stable solid electrolyte interphase (SEI) layer on the anode surface is one of the important factors for higher and more efficient storage performance in batteries. Therefore, we analyzed the formation of the SEI layer on EP Cu-textile through in situ XRD and EIS measurements during the initial GCD cycle (Figs. S24 and S25). The results demonstrate that the EP Cu-textile formed a stable and reversible SEI layer on the surface even during the initial electrochemical sweep, suggesting the high coating quality with uniformity of the EP Cu-textile.

The EP Cu-textile showed much higher current level and more stable CV current responses than the CR Cu-textile and Cu-foil (Figs. 3a, S9 and S11 in the supplementary material), suggesting a larger active surface area with robust structure. We also investigated the galvanostatic charge/discharge (GCD) curves of the 10th cycles of the samples at 0.875 mA cm^{-2} (0.2 C for 10 mg cm^{-2} LTOs) as shown in Fig. 3b. In this case, the areal capacities of the CR Cu-textile and Cu-foil were approximately 0.049 and 0.01 mA h cm^{-2}, respectively. On the other hand, the areal capacity of the EP Cu-textile was measured to be approximately 3.27 mA h cm^{-2}, which was 66.7 and 327 times higher than those of CR Cu-textile and Cu-foil, respectively.

Electrochemical impedance spectroscopy (EIS) was further performed to compare the charge transfer resistance (R_{ct}) values of the current collectors mentioned above. The EP Cu-textile exhibited much lower R_{ct} (~168 Ω) and steeper Warburg slope (i.e., more facile charge
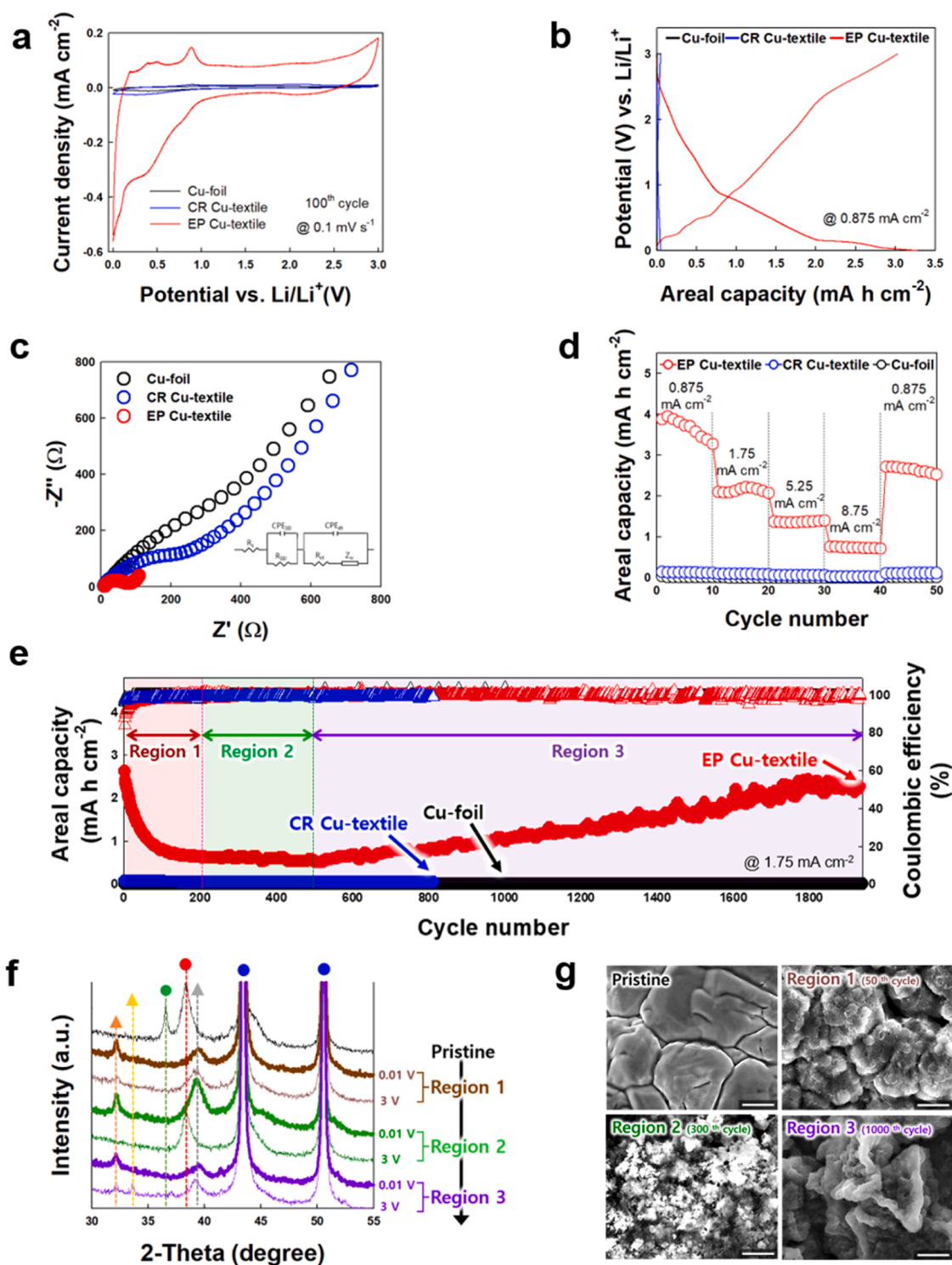
Fig. 3. Electrochemical measurements of Cu-based current collector. (a) CV profiles of EP Cu-textile, CR Cu-textile, and Cu-foil at 0.1 mV s^{-1}. (b) Areal capacities of EP Cu-textile, CR Cu-textile, and Cu-foil at 0.875 mA cm^{-2}. (c) Nyquist plots of EP Cu-textile, CR Cu-textile, and Cu-foil with the corresponding equivalent circuit (inset). (d) Rate capabilities of EP Cu-textile, CR Cu-textile, and Cu-foil at various current densities. (e) Cycling stability and Coulombic efficiency of EP Cu-textile, CR Cu-textile, and Cu-foil at 1.75 mA cm^{-2}. Cycling was separated into 3 stages; fading (Region 1, 0 ~ 200 cycles), reactivation (Region 2, 200 ~ 500 cycles), and negative fading (Region 3, after 500 cycles). (f) *Ex situ*-XRD data for pristine and various regions of fully discharged and charged EP Cu-textiles (● - Cu (JCPDS file No. 04–0836), ● - CuO (JCPDS file No. 48–1548), ● - Cu$_2$O (JCPDS file No. 05–0667, ▲ - Li$_2$O (JCPDS file No. 73–0593), ▲ - LiOH (JCPDS file No. 12–0254), ▲ - Li$_2$O$_2$ (JCPDS file No. 09–0355)). The brown, green and purple lines indicate Region 1, 2, and 3, respectively, while the thick and thin lines correspond to the fully discharged (0.01 V) and charged (3 V) states. (g) FE-SEM images of EP Cu-textile in the pristine and various regions in the fully charged state (scale bar, 500 nm).

transfer) than the other current collectors (Fig. 3c). Furthermore, the rate capabilities of the Cu-based current collectors were evaluated, revealing that the areal capacity of the EP Cu-textile decreased from 3.27 to 0.71 mA h cm^{-2} with increasing the current density from 0.875 to 8.75 mA cm^{-2} (Fig. 3d). When the current density was switched back to 0.875 mA cm^{-2}, the areal capacity was 2.71 mA h cm^{-2}, showing 82.9% capacity retention. Overall, the EP Cu-textile current collector exhibited better rate capability than the CR Cu-textile and Cu foil, reflecting the superior charge transfer behavior and larger active surface area of the EP Cu-textile.

Fig. 3e shows the cycling stabilities of the current collectors at a current density of 1.75 mA cm^{-2}. Our EP Cu-textile exhibited 91.3% ($\sim$2.62 mA h cm^{-2}, Coulombic efficiency $\sim$98.7%) of the initial areal capacity value after $\sim$1900 cycles, while the CR Cu-textile and Cu-foil exhibited 70.0% (800 cycles, 99.0% Coulombic efficiency) and 48.7% (1930 cycles, 103.5%), respectively. Notably, EP Cu-textile recovered its areal capacity after typical capacity degradation (i.e., negative fading effect [47–55]). That is, the EP Cu-textile exhibited 3 stages of behavior during charge/discharge cycling: (1) fading stage at Region 1 (0 $\sim$ 200th cycle), (2) reactivation stage at Region 2 (200th $\sim$ 500th cycle), and (3) negative fading stage at Region 3 (after the 500th cycle). According to *ex situ* XRD, the pristine EP Cu-textile (Fig. 3f) before the cycling test (black line) contained CuO (38.3°), Cu$_2$O (36.5°), and Cu (sharp peaks at 43.4° and 50.5°).

Within Region 1, for the discharged state (0.01 V) of the 50th cycle (thick brown line in Fig. 3f), XRD peaks can be seen for a SEI layer composed of Li$_2$O and LiOH at 32.1° and 39.3°, respectively, while no peaks are visible for CuO (38.3°) or Cu$_2$O (36.5°), which indicates that CuO/Cu$_2$O was completely reduced to Cu with the generation of Li$_2$O/LiOH. Particularly, this SEI layer was continuously formed until all exposed surfaces of the electrode were covered, which strongly depended on the diffusion rate of Li ions [56]. This phenomenon accelerated the rapid decrease in the capacity of electrodes, along with irreversible consumption of large amounts of Li ions at the electrode/electrolyte interface. As the electrode was charged to 3 V (thin brown line in Fig. 3f), the peaks of Li$_2$O and LiOH still remained evidently despite the reduction conversion process. Given that the SEI layer was mainly formed by electrolyte decomposition below 1.0 V, the observed peaks were possibly due to a thick layer of residual SEI phase formed on the electrode surface during the electrochemical sweeps [57–59]. In Region 2 in the 300th cycle (green lines in Fig. 3f), distinct peaks for Li$_2$O (32.1°)/LiOH (39.3°) and CuO (38.3°) reappeared for the discharged and charged states, respectively, implying extensive reversibility of Li$_2$O and LiOH formation in the conversion-type charge storage reaction. By virtue of successive reduction processes, Cu NPs were produced through disintegration of bulk CuO/Cu$_2$O [60], which were embedded in the Li$_2$O matrix, implying the generation of polymeric gel-like layer. The formation/dissolution of such polymeric gel-like layer exhibited conversion-type energy storage behavior, which was also accelerated by Cu NPs with high catalytic activity. In Region 3 (purple lines in Fig. 3f), the discharged state again displayed peaks corresponding to Li$_2$O and LiOH. The intensity of the LiOH peak decreased due to reversible conversion of LiOH to Li$_2$O on the surface, which enhanced the capacity of the EP Cu-textile electrode [50]. In the charged state, the peaks at 32.1°, 33.6°, 38.3°, and 39.3° corresponded to Li$_2$O, Li$_2$O$_2$ [61], CuO and LiOH, respectively.

The negative fading phenomenon of EP Cu-textile during GCD cycling can be further explained using FE-SEM images for each cycle state (Figs. 3g and S12 in the supplementary material). As the cycling processes were proceeded from the 50th cycle in Region 1 to the 300th cycle in Region 2, the initial bulk CuO/Cu$_2$O particles covered with thick/rough SEI layers were disintegrated into NPs. As a result, these phenomena enhanced the Li$^+$/electron transport efficiency and the reactivity with Li ions, and furthermore promoted the reversible transformation of polymeric gel-like layer. Density functional theory (DFT) calculations also revealed that Cu NPs could accelerate the

decomposition of ethylene carbonate and Li$_2$O, thus promoting the facile formation/dissolution of a polymeric gel-like layer (Fig. S13 in the supplementary material). When the cycling process reached the 1,000th cycle in Region 3, a new flower-like irregular 3D structure was observed, which attributed to the Kirkendall effect between the rapid diffusion of Cu ions in the Cu NPs and the relatively slow-diffusion of oxygen ions in the Li$_2$O matrix [47,49,62,63]. This open structure with an increased active surface area exposed more active sites to the electrolyte, which enhanced the electrochemical reactions of the EP Cu-textile, as confirmed by high-resolution transmission electron microscopy (HR-TEM), *ex situ* XPS, CV, and EIS (Figs. S14-S17 in the supplementary material). Negative fading was also observed at a higher current density, resulting in 111.4% ($\sim$ 1.91 mA h cm^{-2}) of the initial areal capacity with 99.4% Coulombic efficiency after $\sim$2500 cycles (Fig. S18 in the supplementary material). Despite its low areal capacity and unstable trend, the behavior of CR Cu-textile was similar to that of EP Cu-textile (Fig. S19 in the supplementary material). However, such similar behavior was not observed in the cycling stability testing of Cu-foil-based anodes. Considering that our EP Cu-textile anode delivered the stably enhanced capacity without additional chemical treatment of the copper oxides, its extremely large surface area with a robust "all-in-one" fibril structure made significant effect on the performance of the anode than those of previously reported CuO-based anodes (Table S1).

2.4. Electrochemical properties of LTO/EP Cu-textile-based anodes

To further confirm the advantage of EP Cu-textile as current collector, Li$_4$Ti$_5$O$_{12}$ (LTO) purchased from Sigma-Aldrich with theoretical capacity of 175 mA h g^{-1}, was used as the active component to prepare an LIB anode. LTO was mixed with poly(vinylidene fluoride) (PVDF) and carbon black (CB, conductive additive) with a weight ratio of 6.5:2.5:1, in N-methyl-2-pyrrolidone (NMP) and deposited on EP Cu-textile by vacuum filtration-assisted doctor-blading method (see Experimental section). The CV was then performed with the LTO/EP Cu-textile electrodes with different mass loadings of LTO at a scan rate of 0.1 mV s^{-1} in the potential range of 0.01–3.0 V (Fig. 4a). As the loading amounts of LTO increased from 5 to 15 mg cm^{-2}, there were notable increases in the intensities of the anodic deintercalation peak at 1.65 V and cathodic peak intercalation peak at 1.49 V; these peaks correspond to typical electrochemical reactions of LTO [64,65]. Additionally, redox peaks originating from the CuO/Cu$_2$O layer (as mentioned above) on the EP Cu-textile were observed. The EP Cu-textile coated with only CB (shortly CB/EP Cu-textile) also showed an increase in the CV current (Fig. S20 in the supplementary material), which was attributed to the reversible lithiation/delithiation in the graphitic planes of CB between 0.01 and 1.5 V [66]. After the CV cycling, the peaks of LTO/EP Cu-textile were stabilized, indicating the reversible lithiation/delithiation of LTO and CB as well as EP Cu-textile (Fig. S21 in the supplementary material).

The electrochemical behaviors of LTO/EP Cu-textile anodes were investigated using The GCD and EIS measurements. The GCD profiles were determined at a current density of 0.875 mA cm^{-2} over the potential range of 0.01–3.0 V (vs. Li/Li$^+$) (Fig. 4b). The profiles exhibited slight voltage plateaus at approximately 1.5–1.6 V, likely originating from phase transitions of LTO during lithiation/delithiation [67]. Notably, the LTO/EP Cu-textile anodes demonstrated an outstandingly high specific capacity of $\sim$573 mA h g^{-2} (at 15 mg cm^{-2} of LTO), significantly exceeding the theoretical capacity of LTO as well as previously reported LTO-based anodes (Table S2). In this case, the mass loading of copper oxide layer on the EP Cu-textile was not include in the calculation of the capacity. As the loading of LTO slurry was increased from 0 to 15 mg cm^{-2}, the areal capacity of the anode was significantly increased from 3.41 to 8.60 mA h cm^{-2}. The Nyquist plots obtained from EIS measurements for the LTO/EP Cu-textile anodes showed that R$_{ct}$ was slightly increased from 168.1 to 303.1 Ω cm^{-2} (Fig. 4c); which indicated facile charge transfer at the electrode/electrolyte interfaces. These
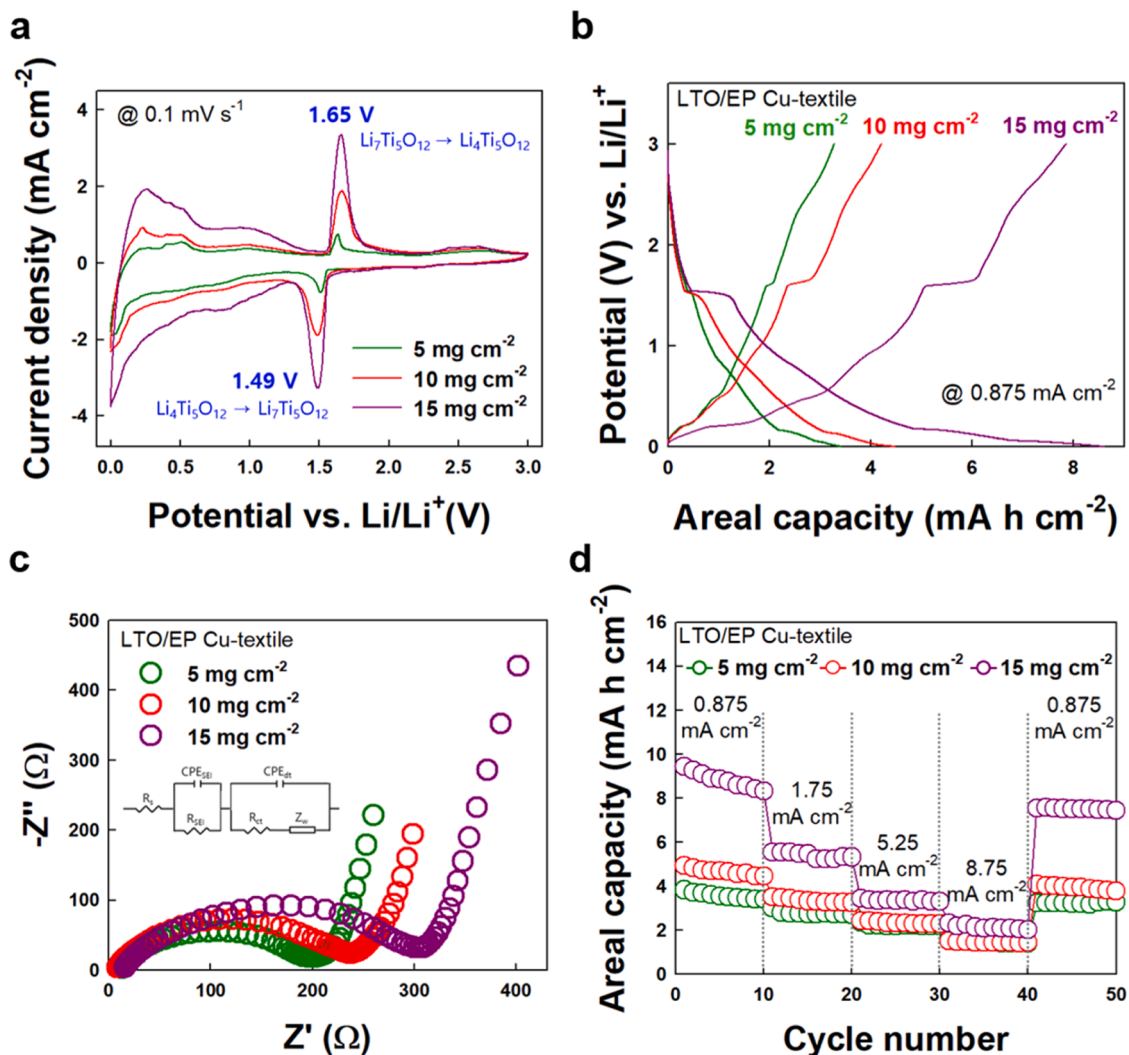
Fig. 4. Electrochemical measurements of LTO/EP Cu-textile electrodes. (a) CV profiles of LTO/EP Cu-textile with LTO loading mass densities of 5, 10, and 15 mg cm^{-2}. (b) GCD profiles of LTO/EP Cu-textile with various LTO loading amounts at 0.875 mA cm^{-2}. (c) Nyquist plots of LTO/EP Cu-textile loaded with different amounts of LTOs and their corresponding equivalent circuit (see the inset). (d) Rate capability of LTO/EP Cu-textile as a function of LTO loading mass at various current densities.

results demonstrated that the EP Cu-textiles could act as active anodes as well as current collectors/energy reservoirs.

The GCD tests were further performed to investigate the rate capabilities of LTO/EP Cu-textile anodes at various current densities (Fig. S28). The charge/discharge profiles after the first 5 cycles were recorded because the first lithiation process during the initial cycles generated the irreversible capacity associated with the formation of SEI layer. The corresponding rates of the EP Cu-textile anodes were shown in Fig. 4d. In the case of LTO/EP Cu-textile anodes with 5 mg cm^{-2} LTO slurry, a high areal capacity of 3.23 mA h cm^{-2} was maintained at 0.875 mA cm^{-2}, which corresponded to 84.3% of the initial areal capacity (i.e., 3.83 mA h cm^{-2} at 0.875 mA cm^{-2}).

2.5. Current collector-dependent electrochemical performance of anodes

Lastly, we investigated how the interfacial structures and electrical conductivities of the Cu-textiles affected the electrochemical performance of the anodes. Slurry (including 10 mg cm^{-2} LTO) was additionally deposited on the CR Cu-textile and Cu-foil. Furthermore, the electrochemical properties of the resulting LTO/CR Cu-textile and LTO/Cu-foil were compared with those of the abovementioned LTO/EP Cu-textile with the same LTO loading. Although the LTO particles were

deeply incorporated in the EP and CR Cu-textiles (Fig. 5a), it should be noted that the Cu layer of CR Cu-textile was considerably nonuniform. These phenomena resulted in the R_{ct} of ~300 Ω, which was higher than R_{ct} (~230 Ω) of the EP Cu-textile electrode as confirmed by EIS measurement (Fig. 5b). However, for the nonporous LTO/Cu-foil anode, the R_{ct} was substantially higher due to the formation of the thicker LTO slurry layer in comparison with that on the EP Cu-textile anodes. That is, the homogeneous distribution of LTO slurry within the EP Cu-textile, containing networks of Cu-plated fibrils, allowed fast and facile access of charge carriers to the LTO surface. In this case, the areal capacities of the LTO/CR Cu-textile and LTO/Cu-foil anodes at different current densities were inferior to that of the LTO/EP Cu-textile anode (Figs. 5c and S29).

We also investigated the rate capabilities of the LTO/EP Cu-textile, LTO/CR Cu-textile, and LTO/Cu-foil with the same loading (10 mg cm^{-2} LTO slurry) (Fig. 5d). In contrast to the LTO/EP Cu-textile, the LTO/CR Cu-textile and LTO/Cu-foil anodes exhibited the relatively small areal capacities as the applied current density was increased from 0.875 to 8.75 mA cm^{-2}, which was mainly caused by the relatively poor ion diffusion efficiency into the nonuniform, thick active layer. Furthermore, the LTO/EP Cu-textile delivered approximately 80.1% (~3.91 mA h cm^{-2}) of the initial areal capacity (~5.22 mA h cm^{-2}) with
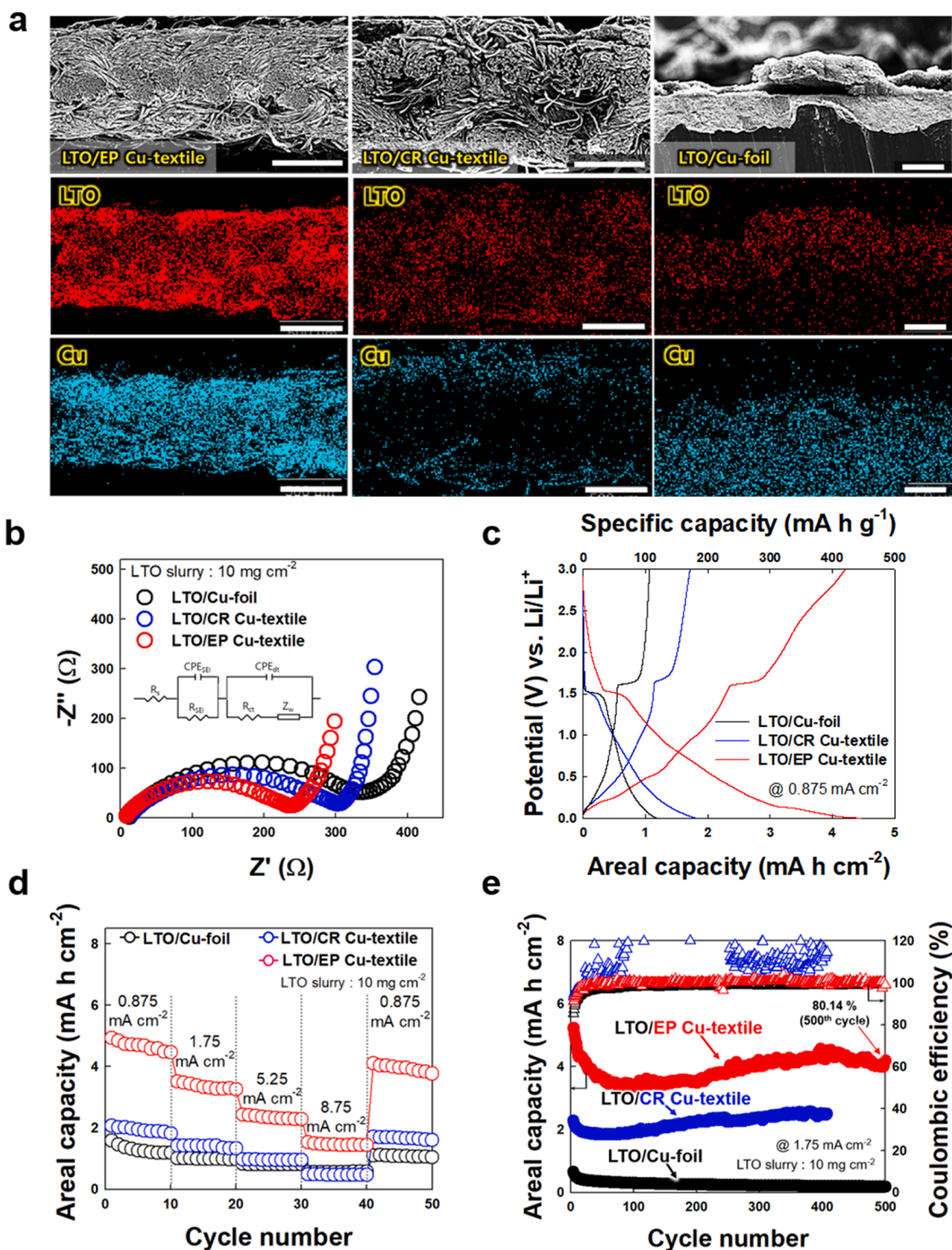
Fig. 5. Electrochemical measurements of LTO/Cu-based electrodes. (a) Cross-sectional FE-SEM images and their corresponding EDS images of LTO/EP Cu-textile, LTO/CR Cu-textile, and LTO/Cu-foil with loading mass densities of 10 mg cm^{-2} (scale bar, 500 nm). (b) Nyquist curves of LTO/EP Cu-textile, LTO/CR Cu-textile, and LTO/Cu-foil (the inset shows the equivalent circuit). (c) GCD profiles of LTO/EP Cu-textile, LTO/CR Cu-textile, and LTO/Cu-foil at 0.875 mA cm^{-2}. (d) Rate capability of LTO/EP Cu-textile, LTO/CR Cu-textile, and LTO/Cu-foil at various current densities. (e) Cycling stability and Coulombic efficiency of LTO/EP Cu-textile, LTO/CR Cu-textile, and LTO/Cu-foil at 1.75 mA cm^{-2}.

a relatively high Coulombic efficiency (99.5%) even after 500 cycles. In contrast, the LTO/CR Cu-textile showed the inferior areal discharge capacity of 2.28 mA h cm^{-2} (109.3% of the initial value) after ~400 charge/discharge cycles at 1.75 mA cm^{-2} (Fig. 5e). Although, during charge/discharge cycling, both the electrodes (i.e., EP Cu-textile and CR Cu-textile electrodes) showed a notable increase in areal capacity due to

the copper oxide layer formed on the electrode surface, the areal capacity of the LTO/Cu-foil anode steadily decreased according to the cycle number without any increase. In this case, the LTO/Cu-foil anode exhibited a low areal capacity of 0.18 mA h cm^{-2} after 530 cycles, which corresponded to 27.1% of the initial areal capacity (at 1.75 mA cm^{-2}). As a result, the EP Cu-textiles enhanced the energy storage performance of

LIB anodes mainly due to their large active surfaces, high electrical conductivities, and robust fibril structures.

3. Conclusion

We successfully prepared EP Cu-textiles with large specific surface area, bulk metal-like electrical conductivity, and excellent structural stability by modifying the surfaces of cotton fibrils. We also demonstrated that the EP Cu-textile itself could be acted as an energy reservoir as well as an electrochemically active current collector with high areal capacity, strong negative fading effect, and long-term cycling stability for LIB anodes. The intrinsic surface area of the cotton textiles was increased by LbL-assembly of MWCNTs and metal NPs on their surface. Additionally, favorable interfacial interactions between cotton textile and conductive layers (i.e., MWCNT, metal NPs, and EP Cu layers) as well as between neighboring conductive layers could maintain the excellent electrical properties of textile electrode under mechanical stress. In particular, the EP Cu-textiles exhibited extremely high areal capacity (3.27 mA h cm^{-2} at 0.875 mA cm^{-2}) with excellent cycling stability (91.3% after ~1900 cycles) due to the continuous formation of catalytic Cu NPs generated by the lithiation-activated formation/dissolution of the polymeric gel-like phase. With increasing the mass loading of LTO slurry on the EP Cu-textile from 5 to 15 mg cm^{-2}, the total areal capacity of anodes increased from approximately 3.27 to 8.60 mA h cm^{-2}, which also showed good rate capability and cycling stability. Additionally, the resulting anode exhibited an unprecedently high specific capacity of ~573 mA h g^{-1} (at 15 mg cm^{-2} LTO), outperforming the theoretical value (~175 mA h g^{-1}) of LTO. This high energy performance was due to the strong contribution of the electrochemically active textile current collector. Our approach based on complementary interactions can provide a basis for developing various high-performance electrochemical electrodes as well as LIB electrodes.

4. Experimental section

4.1. Materials

All chemical reagents were purchased from Sigma-Aldrich and used without further purification. Cotton textile with widths of ≈ 23 μm, and thickness of ≈ 650 μm was purchased from Coasilk (Republic of Korea).

4.2. Synthesis of COOH-MWCNTs

Pristine multiwalled carbon nanotubes (MWCNTs, diameter 7~9 nm, length 10~50 μm, purity>80%, Nanosolution Co. LTD.) were treated with a strongly acidic mixture of H_2SO_4/HNO_3 at 80 °C for 2.5 h. After the reaction, the carboxylic acid-functionalized MWCNTs (COOH-MWCNTs) were thoroughly washed several times by centrifugation and vacuum filtration to remove byproducts and/or acidic residues. The COOH-MWCNTs were then redispersed in ethanol.

4.3. Synthesis of TOABr-Au NPs

Tetraoctylammonium bromide (TOABr)-stabilized Au NPs (TOABr-Au NPs) with a diameter of ~8 nm were synthesized by modifying the Brust-Schiffrin method [68]. In brief, 2 mM of TOABr dispersed in 80 mL of toluene and 30 mM gold (III) chloride trihydrate (HAuCl$_4$·3H$_2$O, Sigma-Aldrich) dissolved in 30 mL of deionized water were mixed and stirred for 10 min. Then, 0.4 M NaBH$_4$ as reducing agent in 20 mL of deionized water was poured into the TOABr/HAuCl$_4$ mixture solution and stirred for 3 h. Finally, the toluene phase was separated from the mixture and washed several times with 0.1 M H_2SO_4 (95% purity, Daejung Chemicals), 0.1 M NaOH (97%, Sigma-Aldrich), and deionized water to eliminate the residual reactants.

4.4. Preparation of Au NP-MWCNT-textile

Dispersion of COOH-MWCNTs in ethanol (2 mg mL^{-1}), TOABr-Au NPs in toluene (5 mg mL^{-1}), and tris(2-aminoethyl)amine (TREN, M$_w$ ~ 146 g mol^{-1}) in ethanol (2 mg mL^{-1}) were prepared for the fabrication of Au NP-MWCNT-textile using an LbL assembly. First, cotton textile composed of hydroxyl (OH)-functionalized cellulose fibrils was dipped into PEI solution for overnight to introduce amine groups on the outermost surface of the textile. After then, amine-functionalized cotton textile was immersed in COOH-MWCNT solution for 10 min. These procedures were repeated to produce MWCNT-coated cotton textile with a desired layer number (n) (i.e., (MWCNT/TREN)$_n$-coated textile, shortly, n-MWCNT-textile). Then, the formed n-MWCNT-textile was successively immersed in TOABr-Au NP solution and TREN solution to form Au NP-MWCNT-textile.

4.5. Preparation of EP Cu-textile

As-prepared Au NP-MWCNT-textile substrate as a cathode and a Cu foil (99.9+%, Sigma-Aldrich) as an anode were connected to an electroplating circuit. The electrodes were dipped into the Cu electroplating solution containing 1000 g L^{-1} copper (II) sulfate pentahydrate (CuSO$_4$·5H$_2$O, Sigma-Aldrich), 50 g L^{-1} sulfuric acid (H$_2$SO$_4$, Sigma-Aldrich), and deionized water. The process of Cu electroplating was conducted for 20 min at 230 mA cm^{-2} using Ivium-n-Stat electrochemical workstation (Ivium Technologies). The Cu-electroplating textile (i.e., EP Cu-textile) was cleaned with deionized water and dried at 120 °C for 4 h in an atmosphere condition.

4.6. Preparation of CR Cu-textile

Cu deposition on cotton textile through chemical reduction (CR) followed the reported procedure [24]. Bare cotton textile was first immersed in dopamine solution (1 mg mL^{-1}, 10 mM Tris buffer; pH = 8.5) for overnight at room temperature. After washing with deionized water, polydopamine coated cotton textile was dipped into (NH$_4$)$_2$PdCl$_4$ (1 mg mL^{-1}) solution for 30 min. Finally, the cotton textile was dipped into plating bath containing a 1:1 mixture of A and B solutions (where A is a mixture of NaOH (12 g L^{-1}), CuSO$_4$·5H$_2$O (13 g L^{-1}), and potassium sodium tartrate (29 g L^{-1}) and B is an aqueous HCHO (9.5 m L^{-1}) solution). After reaction for 1 h, the formed CR Cu-textile was rinsed with deionized water and dried in an atmosphere condition at 120 °C for 4 h.

4.7. Preparation of the slurry coated current collector (LTO/Cu-based current collector and CB/EP-Cu textile)

An active slurry for the LTO/Cu-based current collector was prepared by mechanical blending of LTO powder (average particle diameter of ~200 nm, Sigma-Aldrich), Super P Conductive Carbon Black (MTI Korea), and polyvinylidene fluoride (PVDF, Sigma-Aldrich) with a weight ratio of 6.5:2.5:1; 1-methyl-2-pyrrolidinone (NMP, Sigma-Aldrich) was used as the solvent. While the CB based slurry was prepared by using Super P conductive Carbon Black, and PVDF with a weight ratio of 9:1. The resulting slurries were applied to the EP Cu-textile, CR Cu-textile, and Cu foil by vacuum filtration-assisted doctor-blading method. Briefly, the formed textile current collector was placed on a filtration funnel, and then the LTO slurry was carefully poured onto the textile current collector under vacuum filtration to ensure the uniform coating of the slurry on all surface of the textile. Then, all of the textile electrodes were completely dried at 70 °C in a vacuum oven overnight.

4.8. Characterization

The growth of LbL-assembled multilayers was monitored by Fourier transform infrared (FTIR) analysis using a CARY 600 spectrometer

(Agilent Technologies) in specular mode with a resolution of 4 cm^{-1}, and all spectra were plotted with spectral analysis software (OMNIC, Nicolet). Quartz crystal microgravimetry (QCM 200, SRS) was used to quantitatively measure the growth of multilayer films. Here, the mass change (Δm) of the multilayers was calculated from the frequency change (ΔF) with the Sauerbrey Eq. (1) [69]:

$$\Delta F(Hz) = -56.6 \times \Delta m \tag{1a}$$

Field-emission scanning electron microscopy (FE-SEM) and energy-dispersive X-ray spectroscopy (EDS) images were obtained with a Quanta 250 FEG (FEI) system. X-ray diffraction (XRD) analysis was performed with a SmartLab diffractometer (Rigaku). X-ray photoelectron spectroscopy (XPS) was performed using an X-TOOL (ULVAC-PHI) to analyze the crystallinities of EP Cu-textile. All spectra were calibrated with the C 1 s binding energy peak at 284.6 eV. The mass loading amount of the copper oxide layer on each electrode (i.e., EP Cu-textile, CR Cu-textile, and Cu-foil) was measured through an electropolishing process with a reverse current density of 10 mA cm^{-2} to completely remove the oxide layer. Based on the mass change before and after the process, the areal mass of copper oxides for EP Cu-textile, CR Cu-textile, and Cu-foil was found to be 1.04, 1.48, and 0.37 mg cm^{-2}, respectively.

4.9. Electrochemical measurements

The electrochemical investigations for all electrodes were conducted with coin-type cells (CR2032, MTI Korea) using a WBCS3000 multi-channel workstation. All cells were assembled in an argon-filled glovebox (MBraun, O$_2$ < 0.1 ppm, H$_2$O < 0.1 ppm) using Li foil as counter and reference electrodes and bare cotton as separator. The size of all fabricated electrodes was fixed at 0.5 cm × 0.5 cm (0.25 cm^2). The liquid electrolyte was prepared by dissolving 1 M LiPF6 in a mixture of ethylene carbonate (EC) and dimethyl carbonate (DMC) with a volume ratio of 3:7 containing 10 wt% of FEC additive. The galvanostatic charge-discharge (GCD) performance was evaluated using ZIVE mp2 (WonATech, Republic of Korea) in the voltage range of 0.01 – 3.0 V (vs. Li/Li$^+$) at room temperature. Electrochemical impedance spectroscopy (ESI) measurements were carried out at open circuit voltage in the frequency range of 100 kHz to 0.1 Hz with a perturbation amplitude of 0.01 mV. The preparation of the electrode samples for *ex situ* analysis (including HR-TEM, FE-SEM, and XPS) at the various cycling Regions (i.e., Region 1, 2, and 3 in GCD cycling test) were carried out by disassembling the cell in an argon-filled glovebox immediately after stopping cycling at target stage. In this case, the samples removed from the coin cell were carefully washed several times with DEC and dried at glovebox for less than 2 days. The samples were than sealed to prevent exposure to air before analysis. The total mass of active substance (LTO) loaded to our designated electrodes (i.e., EP Cu-textile, CR Cu-textile, and Cu-foil) were calculated using the following equation:

$$\Delta m \ (mass \ of \ LTO)$$
$$= \{(after \ LTO \ deposited \ EP \ Cu - textile \ weight)$$
$$-(before \ LTO \ deposited \ EP \ Cu)\} \times 0.65$$

4. 10. Computational details

In this work, periodic density functional theory (DFT) calculations were carried out using the Vienna ab initio simulation package (VASP) [70–73]. The projector augmented wave (PAW) method for ion-electron interactions [74,75] and Perdew-Burke-Ernzerhob (PBE) functional within the generalized gradient approximation (GGA) for the exchange-correlation interactions were adopted [76]. The Cu 3d^{10}4s [1], Li 2s [1], C 2s^{2}2p [2], O 2s^{2}2p [4], H 1S [1] electrons were used as valence states, and the spin polarization was included. The DFT-D3 method proposed by Grimme et al. was used to describe van der Waals interactions [77]. The electronic wave functions were expanded to a plane wave basis with a kinetic energy cutoff of 500 eV. The

electronic energy convergence and forces convergence criteria for geometry optimization were set to 1.0×10^{-6} eV and 2.0×10^{-2} eV Å^{-1}, respectively. The Brillouin-zone integration for the Cu(111) slab was sampled on the Monkhorst-Pack scheme with $2 \times 2 \times 1$ meshes of k-points [78]. For the slab models, the bottommost two layers were fixed while the top three layers were fully relaxed. A vacuum region of 20 Å was added to the slab model in the perpendicular direction to the surface to avoid interactions between images due to the periodic boundary conditions. An icosahedron with 55 atoms placed in a 25 Å × 25 Å × 25 Å cell was considered as the nanosized Cu metal particle model and the gamma-centered k-point scheme was used. To search for the activation energy barrier and its corresponding atomic configurations, the climbing image-nudged elastic band (CI-NEB) method was employed with a spring constant of -5.0 eV Å^{-2} and the maximum force criterion on the atoms was set to 5.0×10^{-2} eV Å^{-1} [79,80]. The zero-point energy corrections were taken account into all the total energy calculations.

4. 11. Measurements of oxide layer of the electrodes (EP Cu-textile, CR Cu-textile, and Cu-foil)

The mass loading amount of the native oxide layer of copper in EP Cu-textile, CR Cu-textile, and Cu-foil was measured through an electropolishing process with a reverse current density of 10 mA cm^{-2} to completely remove the oxide layer. Based on the mass change before and after the process, the areal mass of copper oxide for EP Cu-textile, CR Cu-textile, and Cu-foil were found to be 1.04, 1.48, and 0.37 mg cm^{-2}, respectively.

CRediT authorship contribution statement

Euiju Yong: Investigation, Formal analysis, Data curation, Writing – original draft. **Donghyeon Nam:** Investigation, Formal analysis, Data curation, Writing – original draft. **Yangsoo Kim:** Formal analysis. **Kwangsoo Kim:** Formal analysis. **Byung-Hyun Kim:** Formal analysis, Investigation. **Yongmin Ko:** Formal analysis, Data curation, Writing – original draft. **Jinhan Cho:** Conceptualization, Funding acquisition, Supervision, Project administration, Writing – review & editing.

Declaration of Competing Interest

The authors declare that they have no known competing financial interests or personal relationships that could have appeared to influence the work reported in this paper.

Data availability

Data will be made available on request.

Acknowledgments

Supplementary materials

Supplementary material associated with this article can be found, in the online version, at doi:10.1016/j.ensm.2023.102813.

References

[1] M. Li, J. Lu, Z. Chen, K. Amine, 30 Years of Lithium-Ion Batteries, Adv. Mater. 30 (2018), 1800561.
[2] S. Chu, Y. Cui, N. Liu, The path towards sustainable energy, Nat. Mater. 16 (2017) 16–22.

[3] C. Lamiel, I. Hussain, X. Ma, K. Zhang, Properties, functions, and challenges: current collectors, Mater. Today Chem. 26 (2022), 101152.

[4] S. Moitzheim, B. Put, P.M. Vereechen, Advances in 3D thin-film Li-ion batteries, Adv. Mater. Interface. 6 (2019), 1900805.

[5] P. Zhu, D. Gastol, J. Marshall, R. Sommerville, V. Goodship, E. Kendrick, A review of current collectors for lithium-ion batteries, J. Power Source. 485 (2020), 229321.

[6] W. Liu, Z. Chen, G. Zhou, Y. Sun, H.R. Lee, C. Liu, H. Yao, Z. Bao, Y. Cui, 3D porous sponge-inspired electrode for stretchable lithium-ion batteries, Adv. Mater. 28 (2016) 3578–3583.

[7] Y. Yue, H. Liang, 3D current collectors for lithium-ion batteries: a topical review, Small Method. 2 (2018), 1800056.

[8] S. Ha, K.H. Shin, H.W. Park, Y.J. Lee, Flexible Lithium-Ion Batteries with High Areal Capacity Enabled by Smart Conductive Textiles, Small 14 (2018), 1703418.

[9] G. Li, T. Ouyang, T. Xiong, Z. Jiang, D. Adekoya, Y. Wu, Y. Huang, M.-S. Balogun, All-carbon-frameworks enabled thick electrode with exceptional high-areal-capacity for li-ion storage, Carbon N Y 174 (2021) 1–9.

[10] S. Zhou, P. Huang, T. Xiong, F. Yang, H. Yang, Y. Huang, D. Li, J. Deng, M.-S. Balogun, Sub-thick electrodes with enhanced transport kinetics via in situ epitaxial heterogeneous interfaces for high areal-capacity lithium ion batteries, Small 17 (2021), 2100778.

[11] M.-S. Balogun, H. Yang, Y. Luo, W. Qiu, Y. Huang, Z.-Q. Liu, Y. Tong, Achieving high gravimetric energy density for flexible lithium-ion batteries facilitated by core-double-shell electrodes, Energy Environ. Sci. 11 (2018) 1859–1869.

[12] Y. Huang, H. Yang, T. Xiong, D. Adekoya, W. Qiu, Z. Wang, S. Zhang, M.-S. Balogun, Adsorption energy engineering of nickel oxide hybrid nanosheets for high areal capacity flexible lithium-ion batteries, Energy Storage Mater. 25 (2020) 41–51.

[13] L. Wang, T. Wang, L. Peng, Y. Wang, M. Zhang, J. Zhou, M. Chen, J. Cao, H. Fei, X. Duan, J. Zhu, X. Duan, The promises, challenges and pathways to room-temperature sodium-sulfur batteries, Natl. Sci. Rev. 9 (2022) nwab050.

[14] L. Wu, H. Fu, S. Li, J. Zhu, J. Zhou, A.M. Rao, L. Cha, K. Guo, S. Wen, B. Lu, Phase-engineered cathode for super-stable potassium storage, Nat. Commun. 14 (2023) 644.

[15] G. Zhang, X. Li, D. Wei, H. Yu, J. Ye, S. Chen, W. Zhang, J. Zhu, X. Duan, Synergistic engineering of structural and electronic regulation of In$_2$Se$_3$ for ultrastable Li-ion battery, Chem. Eng. J. 453 (2023), 139841.

[16] Q. Huang, D. Wang, Z. Zheng, Textile-based electrochemical energy storage devices, Adv. Energy Mater. 6 (2016) 1600783.

[17] Y. Gao, C. Xie, Z. Zheng, Textile composite electrodes for flexible batteries and supercapacitors: opportunities and challenges, Adv. Energy Mater. 11 (2020), 2002838.

[18] W. Li, M. Li, M. Wang, L. Zeng, Y. Yu, Electrospinning with partially carbonization in air: highly porous carbon nanofibers optimized for high-performance flexible lithium-ion batteries, Nano Energy 13 (2015) 693–701.

[19] Y. Xu, Y. Zhu, F. Han, C. Luo, C. Wang, 3D Si/C fiber paperelectrodes fabricated using a combined electrospray/electrospinning techniquefor Li-ion batteries, Adv. Energy Mater. 5 (2015), 1400753.

[20] A.M. Gaikwad, B.V. Khau, G. Davies, B. Hertzberg, D.A. Steingart, A.C. Arias, A high areal capacity flexible lithium-ion battery witha strain-compliant design, Adv. Mater. 5 (2015), 1401389.

[21] L.K. Ventrapragada, S.E. Creager, A.M. Rao, R. Podila, Carbon nanotubes coated paper as current collectors for secondary Li-ion batteries, Nanotechnol. Rev. 8 (2019) 18–23.

[22] L. Hu, N. Liu, M. Eskilsson, G. Zheng, J. McDonough, L. Wagberg, Y. Cui, Silicon-conductive nanopaper for Li-ion batteries, Nano Energy 2 (2013) 138–145.

[23] Z. Wang, A. Malti, L. Ouyang, D. Tu, W. Tian, L. Wagberg, M.M. Hamedi, Copper-plated paper for high-performance lithium-ion batteries, Small 14 (2018), 1803313.

[24] Y. Yang, Q. Huang, G.F. Payne, R. Sun, X. Wang, A highly conductive, pliable and foldable Cu/cellulose paper electrode enabled by controlled deposition of copper nanoparticles, Nanoscale 11 (2019) 725.

[25] Y. Zhu, M. Yang, Q. Huang, D. Wang, R. Yu, J. Wang, Z. Zheng, D. Wang, V$_2$O$_5$ textile cathodes with high capacity and stability for flexible lithium-ion batteries, Adv. Mater. 32 (2020) 1906205.

[26] J. Chang, J. Shang, Y. Sun, L.K. Ono, D. Wang, Z. Ma, Q. Huang, D. Chen, G. Liu, Y. Cui, Y. Qi, Z. Zheng, Flexible and stable high-energy lithium-sulfur full batteries with only 100% oversized lithium, Nat. Commun. 9 (2018) 4480.

[27] D. Wang, J. Sun, Q. Xue, Q. Li, Y. Guo, Y. Zhao, Z. Chen, Z. Huang, Q. Yang, G. Liang, B. Dong, C. Zhi, A universal method towards conductive textile for flexible batteires with superior softness, Energy Storage Mater. 36 (2021) 272–278.

[28] M. Shi, M. Wu, Z.-.D. Han, S. Li, Y.-.T. Pan, S. Yuan, Q. Wang, Utilization of electroless plating to prepare Cu-coated cotton cloth electrode for flexible Li-ion batteries, Rare Met. 40 (2021) 400–408.

[29] X. Pu, L. Li, H. Song, C. Du, Z. Zhao, C. Jiang, G. Cao, W. Hu, Z.L. Wang, A self-charging power unit by integration of a textile triboelectric nanogenerator and a flexible lithium-ion battery for wearable electronics, Adv. Mater. 27 (15) (2015) 2472.

[30] K. Lee, J.H. Choi, H.M. Lee, K.J. Kim, J.W. Choi, Solution-processed metal coating to nonwoven fabrics for wearable rechargeable batteries, Small 14 (2018), 1703028.

[31] M.V. Reddy, G.V. Subba Rao, B.V.R. Chowdari, Metal oxides and oxysalts as anode materials for li ion batteries, Chem. Rev. 113 (2013) 5364–5457.

[32] K. Jayaramulu, S. Mukherjee, D.M. Morales, D.P. Dubal, A.K. Nanjundan, A. Schneemann, J. Masa, S. Kment, W. Schuhmann, M. Otyepka, R. Zboril, R. A. Fischer, Graphene-based metal-organic framework hybrids for applications in catalysis, environmental, and energy technologies, Chem. Rev. 122 (2022) 17241–17338.

[33] D. Wang, J. Chang, Q. Huang, D. Chen, P. Li, Y.-W.D. Yu, Crumpled, high-power, and safe wearable Lithium-Ion Battery enabled by nanostructured metallic textiles, Fundament. Res. 1 (2021) 399–407.

[34] C. Hwang, W.-J. Song, J.-.G. Han, S. Bae, G. Song, N.-.S. Choi, S. Park, H.-.K. Song, Foldable electrode architectures based on silver-nanowire-wound or carbon-nanotube-webbed micrometer-scale fibers of polyethylene terephthalate mats for flexible lithium-ion batteries, Adv. Mater. 30 (2018), 1705445.

[35] L. Shen, B. Ding, P. Nie, G. Cao, X. Zhang, Advanced energy-storage architectures composed of spinel lithium metal oxide nanocrystal on carbon textiles, Adv. Energy Mater. 3 (2013) 1484–1489.

[36] J. Jiang, P. Nie, B. Ding, W. Wu, Z. Chang, Y. Wu, H. Dou, X. Zhang, Effect of graphene modified Cu current collector on the performance of Li$_4$Ti$_5$O$_{12}$ anode for lithium-ion batteries, ACS Appl. Mater. Interface. 8 (2016) 30926–30932.

[37] A. Sinitskii, A. Dimiev, D.A. Corley, A.A. Fursina, D.V. Kosynkin, J.M. Tour, Kinetics of diazonium functionalization of chemically converted graphene nanoribbons, ACS Nano 4 (2010) 1949.

[38] D.A. Svintsitskiy, A.I. Stadnichenko, D.V. Demidov, S.V. Koscheev, A.I. Boronin, Investigation of oxygen states and reactivities on a nanostructured cupric oxide surface, Appl. Surf. Sci. 257 (2011) 8542–8549.

[39] P. Liang, H. Zhang, Y. Su, Z. Huang, C.-.A. Wang, M. Zhong, *In situ* preparation of a binder-free nano-cotton-like CuO-Cu integrated anode on a current collector by laser ablation oxidation for long cycle life Li-ion batteries, J. Mater. Chem. A 5 (2017) 19781.

[40] Z. Wang, Y. Zhang, H. Xiong, C. Qin, W. Zhao, X. Liu, Yucca fern shaped CuO nanowires on Cu foam for remitting capacity fading of Li-ion battery anodes, Sci. Rep. 8 (2018) 6530.

[41] D. Li, D. Yan, X. Zhang, J. Li, T. Lu, L. Pan, Porous CuO/reduced graphene oxide composites synthesized from metal-organic frameworks as anodes for high-performance sodium-ion batteries, J Colloid Interface Sci. 497 (2017) 350–358.

[42] S.Q. Wang, J.Y. Zhang, C.H. Chen, Dandelion-like hollow microspheres of CuO as anode material for lithium-ion batteries, Scr. Mater. 57 (2007) 337–340.

[43] J. Morales, L. Sanchez, F. Martin, J.R. Ramos-Barrado, M. Sanchez, Nanostructured CuO thin film electrodes prepared by spray pyrolysis: a simple method for enhancing the electrochemical performance of CuO in lithium cells, Electrochim. Acta 49 (2004) 4589–4597.

[44] D.-.W. Zhang, T.-.H. Yi, C.-.H. Chen, Cu nanoparticles derived from CuO electrodes in lithium cells, Nanotechnology 16 (2005) 2338–2341.

[45] Y. Zhu, N. Sun, W. Lin, Y. Ma, C. Lai, Q. Wang, Facile fabrication of three-dimensional hierarchical CuO nanostructures with enhanced lithium storage capability, RSC Adv 5 (2015) 68061.

[46] M.C. Stan, J. Becking, A. Kolesnikov, B. Wankmiller, J.E. Frerichs, M.R. Hansen, P. Bieker, M. Kolek, M. Winter, Sputter coating of lithium metal electrodes with lithiophilic metals for homogeneous and reversible lithium electrodeposition and electrodissolution, Mater. Today 39 (2020) 137–145.

[47] Y.S. Choi, W. Choi, W.-.S. Yoon, J.M. Kim, Unveiling the genesis and effectiveness of negative fading in nanostructured iron oxide anode materials for lithium-ion batteries, ACS Nano 16 (2022) 631–642.

[48] Y. Jiang, D. Zhang, Y. Li, T. Yuan, N. Bahlawane, C. Liang, W. Sun, Y. Lu, M. Yan, Amorphous Fe$_2$O$_3$ as a high-capacity, high-rate and long-life anode material for lithium ion batteries, Nano Energy 4 (2014) 23–30.

[49] H. Sun, G. Xin, T. Hu, M. Yu, D. Shao, X. Sun, J. Lian, High-rate lithiation-induced reactivation of mesoporous hollow spheres for long-lived lithium-ion batteries, Nat. Commun. 5 (2014) 4526.

[50] Y.-.Y. Hu, L.X., K.-.W. Nam, O.J. Borkiewicz, J. Cheng, X. Hua, M.T. Dunstan, X. Yu, K.M. Wiaderek. L.-S. Du, K.W. Chapman, P.J. Chupas, X.-.Q. Yang, C.P. Grey, Origin of additional capacities in metal oxide lithium-ion battery electrodes, Nat. Mater. 12 (2013) 1130–1136.

[51] A. Debart, L. Dupont, P. Poizot, J.-.B. Leriche, J.M. Tarascon, A transmission electron microscopy study of the reactivity mechanism of tailor-made CuO particles toward lithium, J. Electrochem. Soc. 148 (2001) A1266–A1274.

[52] Y. Xu, G. Jian, M.R. Zachariah, C. Wang, Nano-structured carbon-coated CuO hollow spheres as stable and high rate anodes for lithium-ion batteries, J. Mater. Chem. A 1 (2013) 15486.

[53] C. Zhu, D. Chao, J. Sun, I.M. Bacho, Z. Fan, C.F. Ng, X. Xia, H. Huang, H. Zhang, Z. X. Shen, G. Ding, H.J. Fan, Enhanced Lithium Storage Performance of CuO Nanowires by coating of graphene Quantum Dots, Adv. Mater. Interfaces 2 (2015), 1400499.

[54] J.C. Park, J. Kim, H. Kwon, H. Song, Gram-scale synthesis of Cu$_2$O nanocubes and subsequent oxidation to CuO hollow nanostructures for lithium-ion battery anode materials, Adv. Mater. 21 (2009) 803–807.

[55] J. Xu, Y. Liu, L. He, C. Zhang, Y. Zhang, Facile synthesis of CuO mesocrystal/MWCNT composites as anode materials for high areal capacity lithium ion batteries, Ceram. Int. 42 (2016) 12027–12032.

[56] S.J. An, J. Li, C. Daniel, D. Mohanty, S. Nagpure, D.L. Wood III, The state of understanding of the lithium-ion-battery graphite solid electrolyte interphase (SEI) and its relationship to formation cycling, Carbon N Y 105 (2016) 52–76.

[57] D. Aurbach, Review of selected electrode-solution interactions which determine the performance of Li and Li ion batteries, J. Power Source. 89 (2000) 206–218.

[58] P. Verma, P. Maire, P. Novak, A review of the features and analyses of the solid electrolyte interphase in Li-ion batteries, Electrochim. Acta 55 (2010) 6332–6341.

[59] S.-.Y. Lee, K.-.Y. Park, W.-.S. Kim, S. Yoon, S.-.H. Hong, K. Kang, M. Kim, Unveiling origin of additional capacity of SnO$_2$ anode in lithium-ion batteries by realistic *ex situ* TEM anaylsis, Nano Energy 19 (2016) 234–245.

[60] R. Hu, D. Chen, G. Waller, Y. Ouyang, Y. Chen, B. Zhao, B. Rainwater, C. Yang, M. Zhu, M. Liu, Dramatically enhanced reversibility of Li2O in SnO2-based electrodes: the effect of nanostructure on high initial reversible capacity, Energy Environ. Sci. 9 (2016) 595.

[61] Y. Huang, Z. Xu, J. Mai, T.-.K. Lau, X. Lu, Y.-.J. Hsu, Y. Chen, A.C. Lee, Y. Hou, Y. S. Meng, Q. Li, Revisiting the origin of cycling enhanced capacity of Fe_3O_4 based nanostructured electrode for lithium ion batteries, Nano Energy 41 (2017) 426–433.

[62] J.W. Choi, J. McDonough, S. Jeong, J.S. Yoo, C.K. Chan, Y. Cui, Stepwise nanopore evolution in one-dimensional nanostructures, Nano Lett. 10 (2010) 1409–1413.

[63] W. Wang, M. Dahl, Y. Yin, Hollow nanocrystals through the nanoscale Kirkendall effect, Chem. Mater. 25 (2013) 1179–1189.

[64] Z. Yao, X. Xia, C.-a. Zhou, Y. Zhong, Y. Wang, S. Deng, W. Wang, X. Wang, J. Tu, Smart Construction of integrated $CNTs/Li4Ti_5O_{12}$ core/shell arrays with superior high-rate performance for application in lithium-ion batteries, Adv. Sci. 5 (2018), 1700786.

[65] C. Wang, X. Wang, C. Lin, X.S. Zhao, Lithium titante cuboid arrays grown on carbon fiber cloth for high-rate flexible lithium-ion batteries, Small 15 (2019), 1902183.

[66] L. Fransson, T. Eriksson, K. Edstrom, T. Gustafsson, J.O. Thomas, Influence of carbon black and binder on Li-ion batteries, J. Power Source. 101 (2001) 1–9.

[67] T.-.F. Yi, Y. Xie, Y.-.R. Zhu, R.-.S. Zhu, H. Shen, Structural and thermodynamic stability of $Li_4Ti_5O_{12}$ anode material for lihtium-ion battery, J. Power Source. 222 (2013) 448–454.

[68] M. Brust, M. Walker, D. Bethell, D.J. Schiffrin, R. Whyman, Synthesis of thiol derivated gold nanoparticles in a two-phase liquid-liquid system, J. Chem. Soc. Chem. Commun. 0 (1994) 801–802.

[69] D.A. Buttry, Marcel Dekker Inc.: New York, 1991.

[70] G. Kresse, J. Hafner, *Ab initio* molecular-dynamics simulation of the liquid-metal-amorphous-semiconductor transition in germanium, Phys. Rev. B 49 (1994) 14251.

[71] G. Kresse, J. Hafner, *Ab initio* molecular dynamics for liquid metals, Comput. Mater. Sci. 47 (1993) 558.

[72] G. Kresse, J. Furthmüller, Efficiency of ab-initio total energy calculations for metals and semiconductors using a plane-wave basis set, Comput. Mater. Sci. 6 (1996) 15–50.

[73] G. Kresse, J. Furthmüller, Efficient iterative schemes for *ab initio* total-energy calculations using a plane-wave basis set, Phys. Rev. B 54 (1996) 11169.

[74] P.E. Blöchl, Projector augmented-wave method, Phys. Rev. B 50 (1994) 17953.

[75] G. Kresse, D. Joubert, From ultrasoft psudopotentials to the projector augmented-wave method, Phys. Rev. B 59 (1999) 1758.

[76] J.P. Perdew, K. Burke, M. Ernzerhof, Generalized gradient approximation made simple, Phys. Rev. Lett. 77 (1996) 3865.

[77] S. Grimme, Semiempirical GGA-type density functional constructed with a long-range dispersion correction, J. Comput. Chem. 27 (2006) 1787.

[78] H.J. Monkhorst, J.D. Pack, Special points for Brillouin-zone integrations, Phys. Rev. B 13 (1976) 5188.

[79] G. Henkelman, B.P. Uberuaga, H. Jónsson, A climbing image nudged elastic band method for finding saddle points and minimum energy paths, J. Chem. Phys. 113 (2000) 9901.

[80] G. Henkelman, H. Jónsson, Improved tangent estimate in the nudged elastic band method for finding minimum energy paths and saddle points, J. Chem. Phys. 113 (2000) 9978.